

Operando Calorimetry Investigation of Particle Size Effects on Heat Generation in Wadsley–Roth ($W_{0.2}V_{0.8}$) $_3O_7$ -Based Electrodes

Sun Woong Baek, Kira E. Wyckoff, Daniel D. Robertson, Matevž Frajnkovič, Yucheng Zhou, Sarah H. Tolbert, Ram Seshadri, and Laurent Pilon*



Cite This: *ACS Appl. Energy Mater.* 2023, 6, 1355–1367



Read Online

ACCESS |

Metrics & More

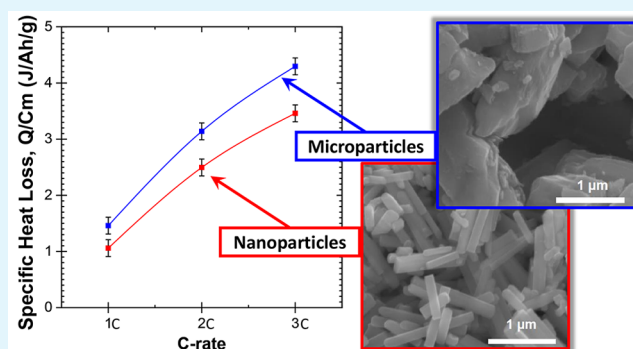
Article Recommendations

Supporting Information

ABSTRACT: The Wadsley–Roth shear phase compound ($W_{0.2}V_{0.8}$) $_3O_7$ is a promising fast-charging electrode material with the ability to engage in multielectron redox reactions and to sustain high specific capacity under large currents. Here, solid-state methods and sol–gel methods combined with freeze-drying were used to synthesize ($W_{0.2}V_{0.8}$) $_3O_7$ microparticles and nanoparticles, respectively. Cyclic voltammetry and galvanostatic cycling demonstrated that electrodes made of ($W_{0.2}V_{0.8}$) $_3O_7$ nanoparticles have superior electrochemical performance compared to those made of microparticles, but the origin of this difference was not well understood. Here, entropic potential measurements performed at slow C-rate indicated that both nanoparticles and microparticles undergo a semiconductor to metal transition.

However, the nanoparticles display a two-phase coexistence over a narrower range of compositions than the microparticles. Operando calorimetry measurements at high C-rate established that, regardless of particle size, the heat generation rate at the ($W_{0.2}V_{0.8}$) $_3O_7$ electrode increased with lithiation due to an increase in charge transfer resistance. The time-averaged irreversible heat generation rate was slightly but systematically smaller at the electrode made of nanoparticles. However, the specific dissipated energy and the contribution from enthalpy of mixing caused by the lithium concentration gradient were notably smaller for the ($W_{0.2}V_{0.8}$) $_3O_7$ nanoparticles. These observations were attributed to the fact that nanoparticles were less ionically resistive and able to accommodate more lithium while lithium-ion intercalation therein was more kinetically favorable.

KEYWORDS: Wadsley–Roth shear phase, Joule heating, reversible heat generation, entropic potential, isothermal calorimetry



1. INTRODUCTION

Since their initial commercialization in the 1990s, lithium-ion batteries (LIBs) have served as the dominant energy source for portable electronics and electric vehicles. In the past decades, significant progress has been made in the development of LIB electrode materials. Different crystallographic structures, such as layered rocksalt-derived lithium cobalt oxide ($LiCoO_2$),¹ olivine lithium iron phosphate ($LiFePO_4$),² and spinel lithium manganese oxide ($LiMn_2O_4$),³ have been developed as electrode materials for commercial batteries. However, for these materials, fast charging is often hindered by the highly anisotropic solid-state diffusivity and by the notable ion path tortuosity associated with some crystal structures.⁴ Alternatively, Wadsley–Roth shear phase compounds have been proposed as electrode materials for fast-charging LIBs. The Wadsley–Roth shear phase compounds typically contain some combination of edge- and corner-shared octahedral, creating open tunnel-like regions through which Li^+ ions can rapidly diffuse during lithiation and delithiation.^{5–7} Furthermore, nuclear magnetic resonance (NMR) as well as magnetism and conductivity measurements have demonstrated that

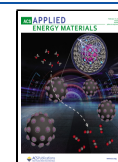
Wadsley–Roth shear phase materials have low activation barriers favorable to fast lithium diffusion.^{8,9} Among materials with Wadsley–Roth crystallographic shear structure, tungsten vanadium oxide ($W_{0.2}V_{0.8}$) $_3O_7$ is a promising fast-charging electrode material due to its ability to engage in multielectron redox reactions and to sustain high specific capacity under large currents.¹⁰ Moreover, vanadium is more abundant than niobium. Thus, vanadium-based ($W_{0.2}V_{0.8}$) $_3O_7$ is an interesting alternative to the niobium-based Wadsley–Roth shear phase materials.¹⁰

In addition to the new crystallographic framework offered by Wadsley–Roth shear phase compounds, mesoscale and nanoscale structuring of their particle morphology can further enhance their fast-charging ability by decreasing the Li-ion

Received: September 26, 2022

Accepted: January 3, 2023

Published: January 27, 2023



diffusion lengths within the particles. In our previous work, we demonstrated that electrodes made from $(W_{0.2}V_{0.8})_3O_7$ nanoparticles showed better rate capabilities than those made from microparticles of the same compounds.¹⁰

Conventional electrochemical characterization methods, such as galvanostatic cycling and cyclic voltammetry, can give insight into the charging mechanisms taking place in battery materials during cycling. However, those methods are not able to identify subtle changes in bonding or structure which can in turn have a dramatic effect on the material's electrical conductivity and thermodynamic properties. Therefore, alternative or complementary characterization techniques are desirable to further observe and understand the physicochemical phenomena occurring in battery electrodes upon cycling. One particularly useful method is potentiometric entropy measurements which can shed light on the entropic changes occurring in the electrode materials and thus provide a window into structural changes including phase transition and ion ordering.¹¹ A second highly informative method is *operando* calorimetry, which is capable of directly measuring the instantaneous heat generation rate in each electrode of a battery cell during charging/discharging and thus can provide insights into the different phenomena contributing to energy dissipation upon charging/discharging.^{12,13}

The present study aims to use potentiometric entropy and calorimetric measurements to understand structural changes and different physicochemical phenomena occurring in $(W_{0.2}V_{0.8})_3O_7$ working electrodes made of particles with different sizes during cycling. Potentiometric entropy measurements at low C-rates were combined with other electrochemical characterization techniques to investigate the phase transition occurring in the $(W_{0.2}V_{0.8})_3O_7$ electrodes. Furthermore, the instantaneous heat generation rates were measured by *operando* isothermal calorimetry at high C-rate in the electrode made of $(W_{0.2}V_{0.8})_3O_7$ microparticles or nanoparticles with lithium metal counter electrodes in 1 M of $LiPF_6$ in EC:DMC 1:1 v/v during cycling. These measurements were used to gain insight into the dynamic interfacial and transport phenomena responsible for any energy dissipation upon cycling.

2. BACKGROUND

2.1. Entropic Potential Measurements. Entropic potential measurement methods aim to measure the open-circuit voltage $U_{ocv}(x, T)$ and the entropic potential $\partial U_{ocv}(x, T)/\partial T$ for a given lithium composition x . Based on the Nernst equation, the open-circuit voltage $U_{ocv}(x, T)$ of a battery cell consisting of a $(W_{0.2}V_{0.8})_3O_7$ -based working electrode and a metallic Li counter electrode can be expressed as^{11,14}

$$U_{ocv}(x, T) = -\frac{\mu_{Li}^{WVO}(x, T) - \mu_{Li}^o(T)}{e} \quad (1)$$

Here, e is the unit charge, and $\mu_{Li}^{WVO}(x, T)$ and $\mu_{Li}^o(T)$ are the Li chemical potentials in the $(W_{0.2}V_{0.8})_3O_7$ working electrode and at the metallic Li counter electrode, respectively. Our previous study¹¹ has demonstrated the relationships between $U_{ocv}(x, T)$ or $\partial U_{ocv}(x, T)/\partial T$ and the materials' thermodynamic properties. We also provided an interpretative guide to $U_{ocv}(x, T)$ and $\partial U_{ocv}(x, T)/\partial T$ plotted as functions of lithium composition x during lithiation or delithiation for intercalation compounds cycled against a metallic Li counter electrode

treated as an infinite lithium reservoir. Neglecting the contributions from surface energy of the pure metallic Li counter electrode, $\partial U_{ocv}(x, T)/\partial T$ can be written as¹¹

$$\frac{\partial U_{ocv}(x, T)}{\partial T} = \frac{1}{e} \left[\frac{\partial s_{WVO}(x, T)}{\partial x} - s_{Li}^o(T) \right] \quad (2)$$

where $s_{WVO}(x, T)$ and $s_{Li}^o(T)$ are the normalized entropy per mole of $(W_{0.2}V_{0.8})_3O_7$ or metallic Li, respectively. Here, $s_{Li}^o(T)$ is independent of x at any given pressure and temperature and was reported to be 29 J/(mol K) at room temperature.¹⁵ Thus, the trend of $\partial U_{ocv}(x, T)/\partial T$ is dependent on the partial molar entropy of $(W_{0.2}V_{0.8})_3O_7$, denoted by $\partial s_{WVO}(x, T)/\partial x$. Therefore, measuring $\partial U_{ocv}(x, T)/\partial T$ during cycling can provide insights into physicochemical phenomena occurring in the $(W_{0.2}V_{0.8})_3O_7$ particles of the working electrode that result in entropy change during lithiation and delithiation.

2.2. Calorimetry. Several calorimetric measurement techniques have been used to probe heat generation associated with battery operation and electrical energy losses. For instance, differential scanning calorimetry,^{16,17} accelerating rate calorimetry,^{18,19} and *operando* isothermal calorimetry^{5,20} have been used to develop thermal management systems to prevent thermal runaway¹⁹ and to investigate transport processes as well as chemical reactions occurring during battery cycling.^{5,20} Furthermore, our previous *operando* isothermal calorimetry studies using a custom-made calorimeter capable of measuring the instantaneous heat generation rates¹² have revealed thermal signatures associated with a variety of physicochemical phenomena including ion adsorption/desorption in supercapacitors,^{21–24} electrolyte decomposition at high voltages and/or high temperatures,^{22,25} ion intercalation,²² overscreening effects,^{25,26} resistive losses,^{5,21–24} and insulator to metal transition.⁵ In the present study, an *operando* isothermal calorimeter was used to investigate the energy dissipation mechanisms in $(W_{0.2}V_{0.8})_3O_7$ electrodes during cycling and the effect of particle size on heat generation.

The total instantaneous heat generation rate $\dot{Q}_T(x, T)$ (in W) in a two-electrode cell can be divided into four contributions, namely, (1) Joule heating $\dot{Q}_J(x, T)$, (2) reversible entropic heat generation $\dot{Q}_{rev}(x, T)$, (3) enthalpy of mixing $\dot{Q}_{mix}(x, T)$, and (4) heat generation due to side reactions $\dot{Q}_{sr}(x, T)$. Thus, $\dot{Q}_T(x, T)$ can be expressed as^{5,20,27,28}

$$\dot{Q}_T = \dot{Q}_J + \dot{Q}_{rev} + \dot{Q}_{mix} + \dot{Q}_{sr} \quad (3)$$

where $\dot{Q}_T(x, T)$ is negative when the electrode absorbs heat and positive when it releases heat.

Under isothermal conditions, the exothermic Joule heating $\dot{Q}_J(x, T)$ associated with irreversible resistive losses can be written as^{5,20,27,28}

$$\dot{Q}_J(x, T) = I[V(x, T) - U^{avg}(x, T)] \quad (4)$$

Here, I is the applied current, and $U^{avg}(x, T)$ is the open-circuit voltage evaluated at the volume-averaged concentration of lithium ions in the cell, considering a single electrochemical reaction.²⁹ Specifically, $U^{avg}(x, T)$ is "the potential to which the cell would relax if the current was interrupted".²⁸ In practice, $U^{avg}(x, T)$ can be measured using GITT at the same C-rate as that used for the calorimetric measurements, provided that the

materials can cycle sufficiently fast. In addition, $[V(x, T) - U^{\text{avg}}(x, T)]$ is the so-called battery overpotential corresponding to the voltage drop due to internal resistance.

In addition, the reversible entropic heat generation rate $\dot{Q}_{\text{rev}}(x, T)$ associated with the changes in the entropy of the battery upon cycling can be expressed as^{20,27,28}

$$\dot{Q}_{\text{rev}}(x, T) = IT \frac{\partial U^{\text{avg}}(x, T)}{\partial T} \quad (5)$$

Under extremely small current, Li is uniformly distributed within the cell, and the operating voltage $V(x, T)$ is equal to the open-circuit voltage $U_{\text{ocv}}(x, T)$, i.e., $V(x, T) = U^{\text{avg}}(x, T) = U_{\text{ocv}}(x, T)$. Then, $\dot{Q}_{\text{J}}(x, T) \approx 0$, and heat generation is solely due to $\dot{Q}_{\text{rev}}(x, T)$.³⁰ However, under high current, $\dot{Q}_{\text{J}}(x, T)$ dominates,³⁰ and Li concentration gradients form within the working electrode and electrolyte due to mass transport resistance.

The heat generation rate from enthalpy of mixing $\dot{Q}_{\text{mix}}(x, T)$ due to the ion concentration gradients in the working electrode and electrolyte caused by diffusion limitation in the LIB can be written as^{20,27,28}

$$\dot{Q}_{\text{mix}}(x, T) = \int_{V_{\infty}} \sum_i [\bar{h}_i(x, T) - \bar{h}_i^{\text{avg}}(x, T)] \frac{\partial c_i}{\partial t} dV \quad (6)$$

Here, V_{∞} is the volume of the cell, and c_i is the local concentration of ion species i . In addition, $\bar{h}_i(x, T)$ and $\bar{h}_i^{\text{avg}}(x, T)$ are the local and volume-averaged partial molar enthalpy of ion species i , respectively. The enthalpy of mixing is mainly caused by four different ionic concentration gradients: (i) across the electrolyte due to mass transfer resistance, (ii) across the electrode caused by nonuniform current distribution, (iii) within vacancies of the electrode, and (iv) within intercalated Li in the electrode due to electrochemical reactions.^{29,31} In general, the ionic concentration gradient of the intercalated Li in the electrode is the dominant contribution to the enthalpy of mixing in LIBs.²⁸ Thus, if the transport of a Li^+ ion in the electrode is fast, $\dot{Q}_{\text{mix}}(x, T)$ should remain small.

Most calorimetry studies on LIBs have neglected the heat generation caused by the side reaction $\dot{Q}_{\text{sr}}(x, T)$ because most undesirable side reactions are prevented by cycling the device in an appropriate potential range.^{20,27,28,32} Then, the aging process of LIBs occurs at relatively slow rates,²⁷ and the associated $\dot{Q}_{\text{sr}}(x, T)$ is negligible compared to $\dot{Q}_{\text{J}}(x, T)$, $\dot{Q}_{\text{rev}}(x, T)$, and $\dot{Q}_{\text{mix}}(x, T)$ early in the LIB's life.²⁰

The total thermal energy Q_{T} (in J) dissipated over a charging/discharging cycle as well as the heat released in the form of Joule heating Q_{J} and enthalpy of mixing Q_{mix} can be calculated as²⁰

$$Q_i = \oint_{\text{cycle}} \dot{Q}_i(x, T) dt \quad \text{with } i = T, J, \text{ rev, or mix} \quad (7)$$

Note that integrating the reversible heat generation rate $\dot{Q}_{\text{rev}}(x, T)$ with respect to time over a cycle yields zero, i.e., $Q_{\text{rev}} = 0$.

Finally, the net electrical energy losses ΔE_e (in J) over a charging/discharging cycle is the difference between the electrical energy delivered during charging and that recovered

during discharging. Graphically, ΔE_e is the area enclosed by the hysteric voltage $V(x, T)$ vs the charge transferred q and can be written as^{5,20}

$$\Delta E_e = \oint_{\text{cycle}} V(x, T) dq = \oint_{\text{cycle}} V(x, T) I dt \quad (8)$$

Here, I is the current such that $I = dq/dt$. Based on the first law of thermodynamics, the total thermal energy Q_{T} dissipated during a cycle is equal to the net electrical energy loss ΔE_e , i.e.

$$\Delta E_e = Q_{\text{J}} + Q_{\text{mix}} = Q_{\text{T}} \quad (9)$$

This relationship has been validated experimentally with LIBs with electrodes made of TiNb_2O_7 ,⁵ $\text{PNb}_9\text{O}_{25}$,¹³ and $\text{Ti}_2\text{Nb}_2\text{O}_9$.³³

3. MATERIALS AND METHODS

3.1. Synthesis of $(\text{W}_{0.2}\text{V}_{0.8})_3\text{O}_7$ Powders. The solid-state preparation of $(\text{W}_{0.2}\text{V}_{0.8})_3\text{O}_7$ microparticles followed the synthesis described in ref 10. In brief, the material was prepared by heating a stoichiometric mixture of precursor oxide powders of WO_3 , V_2O_5 , and V_2O_3 to 700 °C for 24 h in a sealed vitreous silica tube backfilled with a partial pressure of argon. After annealing, the tube was water quenched to room temperature to obtain $(\text{W}_{0.2}\text{V}_{0.8})_3\text{O}_7$ microparticles.

The $(\text{W}_{0.2}\text{V}_{0.8})_3\text{O}_7$ nanoparticles were prepared by combining sol-gel synthesis with a freeze-drying method. First, 200 mg of NH_4VO_3 and 105 mg of $(\text{NH}_4)_{10}(\text{H}_2\text{W}_{12}\text{O}_{42})$ were added to 4 mL of distilled water and heated while stirring until the solids were fully dissolved. The resulting yellow solution was added dropwise to liquid nitrogen. After the removal of the remaining liquid nitrogen, the frozen solution was subjected to vacuum (<100 mTorr) on a Schlenk line for 10–20 h to remove water. The dried powder was calcined in a tube furnace with flowing Ar with a heat ramp of 30 °C/min followed by a 1 h hold at 700 °C. The furnace was then cooled to room temperature. The synthesized nanoparticles were stored under an inert atmosphere to prevent unwanted surface oxidation.

Finally, the $(\text{W}_{0.2}\text{V}_{0.8})_3\text{O}_7$ particles, synthesized by solid-state or sol-gel syntheses, were characterized with an FEI Apreo C scanning electron microscope (SEM) with a voltage of 15 kV and a current of 0.8 nA.

3.2. Electrode and Device Fabrication. The same procedure was followed to fabricate working electrodes made of the $(\text{W}_{0.2}\text{V}_{0.8})_3\text{O}_7$ powders synthesized by either solid-state or freeze-drying methods, as described previously. First, the synthesized $(\text{W}_{0.2}\text{V}_{0.8})_3\text{O}_7$ powder was ball-milled using a vortex mixer (Genie, Vortex-Genie) for 20 min in a 2 cm³ canister with SuperP (TIMCAL) and carbon nanotubes (CNTs). Then, the mixture was combined with poly(vinylidene fluoride) (PVDF) dissolved in *N*-methyl-2-pyrrolidone (NMP) to form a slurry with a mass ratio 8:0.5:0.5:1 of $(\text{W}_{0.2}\text{V}_{0.8})_3\text{O}_7$:Super P:CNT:PVDF. The slurry was thoroughly mixed using the vortex mixer for 30 min before casting. A doctor blade set to 250 μm was used to cast the slurry onto a copper foil current collector. The electrode was dried in a vacuum oven at 110 °C overnight. Then, electrodes were punched into a 10 mm diameter disc for coin cell fabrication. For calorimetry, the electrodes were cut into a 1 × 1 cm² square shape with a 4 cm × 0.25 cm strip current collector, as described previously.¹² The mass loading of the active material in electrodes made of $(\text{W}_{0.2}\text{V}_{0.8})_3\text{O}_7$ microparticles and nanoparticles was in the range of 6–7 mg/cm². All coin cells were fabricated in an Ar-filled glovebox using 2032 SS casings (MTI parts). They consisted of a $(\text{W}_{0.2}\text{V}_{0.8})_3\text{O}_7$ electrode with 1 M of LiPF_6 in EC:DMC 1:1 v/v (Sigma-Aldrich) as the electrolyte, polished metallic lithium (Sigma-Aldrich) ribbon as the counter electrode, and a 50 μm thick Celgard C380 polypropylene/polyethylene separator. Cyclic voltammetry, galvanostatic cycling, and potentiometric entropy measurements were performed on the coin cells using a high accuracy potentiostat (Biologic, VSP-300) in the voltage range of 1.0–3.0 V.

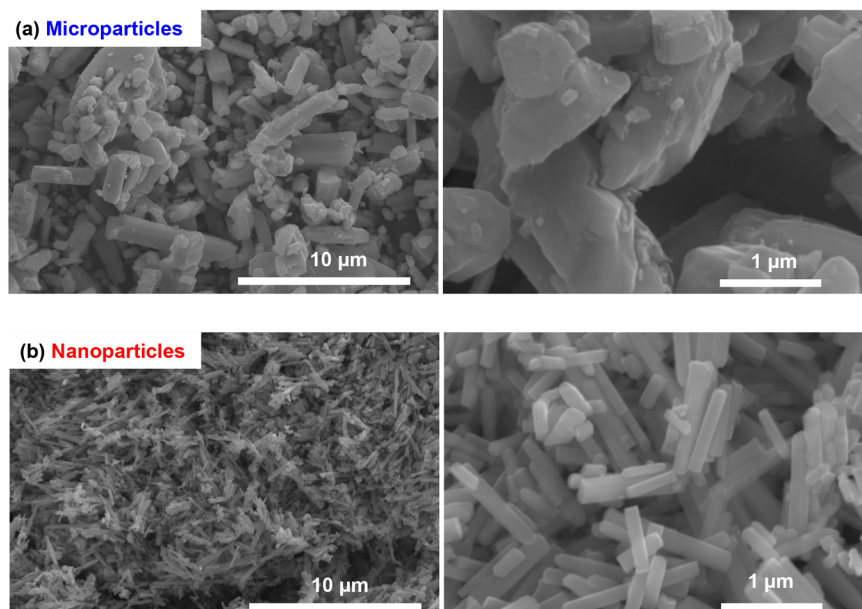


Figure 1. Scanning electron microscope images of (a) $(W_{0.2}V_{0.8})_3O_7$ microparticles synthesized by the solid-state method and (b) nanoparticles made by sol-gel synthesis combined with the freeze-drying method.

3.3. Potentiometric Entropy Measurements. The open-circuit voltage $U_{ocv}(x, T)$ and the entropic potential $\partial U_{ocv}(x, T)/\partial T$ of the coin cells were measured as functions of lithium composition x using the potentiometric entropy measurement technique and the apparatus previously described in ref 5. In brief, the measurements consisted of imposing a series of constant current pulses at a C-rate of C/10 at 20 °C. Each current pulse lasted for 30 min followed by a relaxation period of 90 min. During the relaxation period, the temperature of the coin cell was varied from 15 to 25 °C in 5 °C increments using a thermoelectric cold plate (TE technology, CP-121) in contact with the coin cell. The corresponding coin cell voltage evolution was recorded with a high accuracy potentiostat (Biologic, VSP-300). The lithium composition x in $Li_x(W_{0.2}V_{0.8})_3O_7$ can be estimated based on the charging/discharging time t (in s), i.e.,

$$x = \frac{It}{3600MC_{theo}} \quad (10)$$

where M is the mass loading of the active material in the electrode, and C_{theo} is the theoretical capacity of $(W_{0.2}V_{0.8})_3O_7$ calculated as $C_{theo} = 230$ mAh/g based on one electron per transition metal. In addition, $U^{avg}(x, T)$ and $\partial U^{avg}(x, T)/\partial T$ were also measured using the same procedure and the same relaxation time as that used for measuring $U_{ocv}(x, T)$ but with current pulses corresponding to different C-rates. In addition, the duration of the current pulses changed with C-rates such that, at a C-rate of 1C, each current pulse lasted 3 min, while it lasted 2 min at 2C, and 1 min at 3C. Regardless of the C-rate, we verified that the coin cell had reached thermodynamic equilibrium before imposing the next temperature step during the relaxation period. To do so, we verified that (i) the temperature difference between the cold plate and the top of the coin cell surface was less than 0.1 °C and (ii) the time rate of change of the open-circuit voltage $\partial U_{ocv}(x, T)/\partial t$ or $\partial U^{avg}(x, T)/\partial t$ was less than 5 mV/h.

3.4. Operando Isothermal Calorimetry. The instantaneous heat generation rates at the $(W_{0.2}V_{0.8})_3O_7$ working electrode and at the metallic lithium counter electrode were measured separately under galvanostatic cycling using a custom-made isothermal calorimeter described previously.¹² The calorimetric cell consisted of (i) a 1×1 cm² $(W_{0.2}V_{0.8})_3O_7$ -based electrode, (ii) two 50 μm thick Celgard C380 polypropylene/polyethylene separator sheets, (iii) 1 M LiPF₆ in EC:DMC 1:1 v/v (Sigma-Aldrich) as the electrolyte, and (iv) polished metallic lithium (Sigma-Aldrich) as the counter electrode.

Here, the mass loading of the active material in the electrode made of $(W_{0.2}V_{0.8})_3O_7$ microparticles and nanoparticles was 6.5 mg/cm² and 6.9 mg/cm², respectively. As discussed in ref 12, the heat generation rate $\dot{Q}_i(t)$ (in mW) at each electrode was equal to the heat transfer rate $q_i''(t)$ measured at the 1×1 cm² thermoelectric heat flux sensor (greenTEG, gSKIN-XP) placed in thermal contact with the back of each electrode, i.e.,¹²

$$\dot{Q}_i(t) = q_i''(t)A_i = \frac{\Delta V_i(t)}{S_i}A_i \quad \text{with } i = \text{WVO or Li} \quad (11)$$

Here, A_i is the footprint area of the electrode (in cm²), ΔV_i is the voltage difference measured at each heat flux sensor, and S_i is the sensitivity of the heat flux sensor (in μV/(W/cm²)). The total instantaneous heat generation rate in the entire calorimetric cell can be expressed as the sum of the heat generation rate measured at each electrode, i.e., $\dot{Q}_t(t) = \dot{Q}_{Li}(t) + \dot{Q}_{WVO}(t)$. The instantaneous heat generation rate $\dot{Q}_i(t)$ at electrode “ i ” can be divided into an irreversible $\dot{Q}_{irr,i}(t)$ and a reversible $\dot{Q}_{rev,i}(t)$ contribution, i.e.,

$$\dot{Q}_i(t) = \dot{Q}_{irr,i}(t) + \dot{Q}_{rev,i}(t) \quad \text{with } i = \text{WVO or Li} \quad (12)$$

Here, $\dot{Q}_{irr,i}(t)$ may vary with time as the electrical and/or ionic conductivities of the electrode may change upon charging/discharging, for example.⁵ However, $\dot{Q}_{rev,i}(t)$ averaged over an entire cycle should yield zero due to its reversible nature. Therefore, the time-averaged irreversible heat generation rate $\bar{Q}_{irr,i}(t)$ at electrode “ i ” can be calculated according to

$$\bar{Q}_{irr,i} = \frac{1}{t_{cd}} \oint_{\text{cycle}} \dot{Q}_i(t) dt \quad \text{with } i = \text{WVO or Li} \quad (13)$$

where t_{cd} is the cycle period.

4. RESULTS AND DISCUSSION

4.1. Material and Electrochemical Characterization.

Figure 1 shows the SEM images of the two types of $(W_{0.2}V_{0.8})_3O_7$ particles synthesized in this study. Both types of particles featured a rod-like morphology consistent with earlier observations.³⁴ Figure 1(a) indicates that the average particle size of $(W_{0.2}V_{0.8})_3O_7$ particles synthesized by the solid-

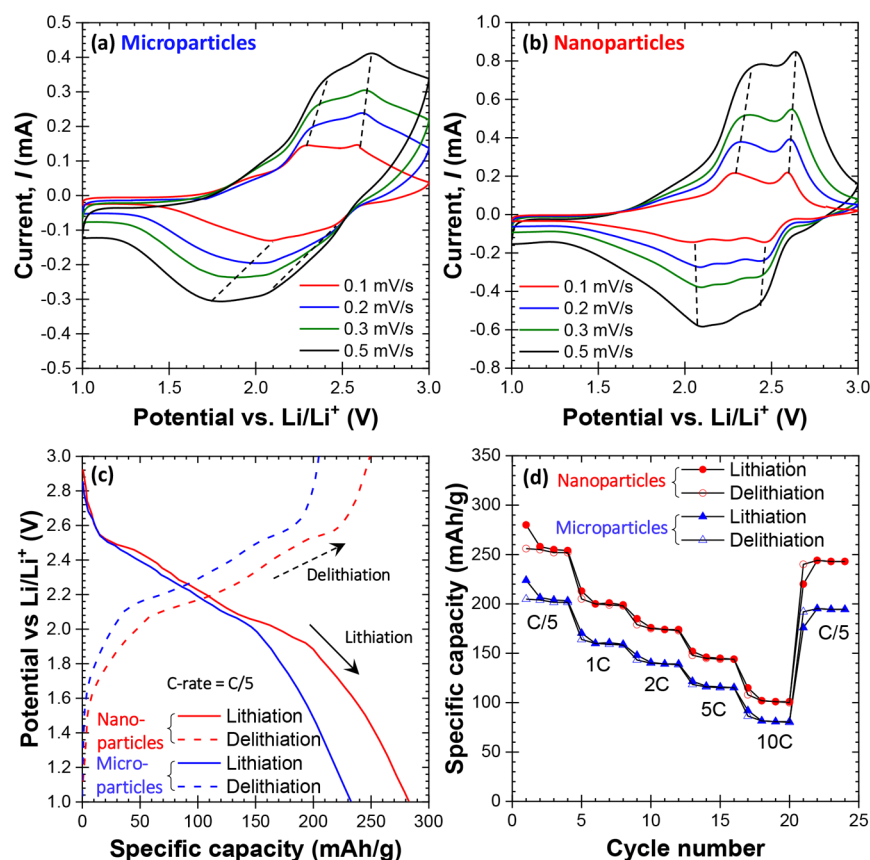


Figure 2. Cyclic voltammogram of the cell containing electrodes made of $(W_{0.2}V_{0.8})_3O_7$ in the form of (a) microparticles synthesized by the solid-state method and of (b) nanoparticles from sol–gel with the freeze-drying method cycled with a potential window ranging from 1.0 to 3.0 V vs Li/Li⁺ at different scan rates ν , (c) galvanostatic charge–discharge potential profile at C-rate of C/5, and (d) specific capacity retention of the cell cycled between 1.0 and 3.0 V vs Li/Li⁺ at C-rates between C/5 and 10C.

state method was around 1–2 μm with lengths ranging from 1 to 10 μm . On the other hand, Figure 1(b) shows that the rods synthesized by the freeze-drying method were about 100 nm wide and 1–2 μm in length. Furthermore, X-ray diffraction (XRD) spectroscopy data of the two types of particles were presented in our previous paper and confirmed that the desired phase was obtained.¹⁰ These results were confirmed by X-ray fluorescence (XRF) spectrometry measurements (see Table S1 of Supporting Information).

Figures 2(a) and 2(b) show cyclic voltammograms at scan rates ν between 0.1 and 0.5 mV/s for a potential window between 1.0 and 3.0 V vs Li/Li⁺ for electrodes made of $(W_{0.2}V_{0.8})_3O_7$ microparticles and nanoparticles, respectively. Both $(W_{0.2}V_{0.8})_3O_7$ -based electrodes showed 4 redox peaks at similar potentials at the relatively low scan rate $\nu = 0.1$ mV/s. As the scan rate increased, the redox peaks for the electrode made of $(W_{0.2}V_{0.8})_3O_7$ microparticles shifted significantly compared to that of nanoparticles and were not as sharp. This can be attributed to the fact that the redox reactions were more kinetically limited in the microparticles than in the nanoparticles. The b -values associated with each cathodic and anodic peak were obtained by fitting the peak current I_{peak} vs scan rate ν with the power law $I_{\text{peak}} = a\nu^b$ (see Supporting Information).³⁵ Table 1 reports the potential and the associated b -value corresponding to each redox peak for electrodes made of $(W_{0.2}V_{0.8})_3O_7$ microparticles and nanoparticles. For both types of electrodes, all cathodic and anodic peaks featured a b -

Table 1. Potential and b -Values of Redox Peaks in the Cyclic Voltammometry Curve for Electrodes Made of $(W_{0.2}V_{0.8})_3O_7$ Microparticles and Nanoparticles

	Microparticles		Nanoparticles	
	Potential (V)	b -value	Potential (V)	b -value
Oxidation peaks	2.26	0.55	2.19	0.62
	2.58	0.56	2.52	0.64
Reduction peaks	2.08	0.57	2.01	0.63
	2.46	0.52	2.47	0.58

value close to 0.5, suggesting that charging and discharging were limited by diffusion. As such, $(W_{0.2}V_{0.8})_3O_7$ behaved as a traditional battery material.³⁶ Interestingly, the calculated b -values for the electrode made of $(W_{0.2}V_{0.8})_3O_7$ nanoparticles were systematically larger, albeit only slightly, than those of the electrode made of microparticles, suggesting that redox reactions were slightly less diffusion-limited in nanoparticles than microparticles.³⁶

Figure 2(c) shows the galvanostatic charge–discharge potential profile at a C-rate of C/5 of coin cells containing electrodes composed of $(W_{0.2}V_{0.8})_3O_7$ microparticles or nanoparticles between 1.0 and 3.0 V vs Li/Li⁺. The trends in the voltage curves of both coin cells were similar during lithiation and delithiation. However, the specific capacity of the cell with the electrode made of $(W_{0.2}V_{0.8})_3O_7$ nanoparticles was 280 mAh/g compared with 230 mAh/g for that made of

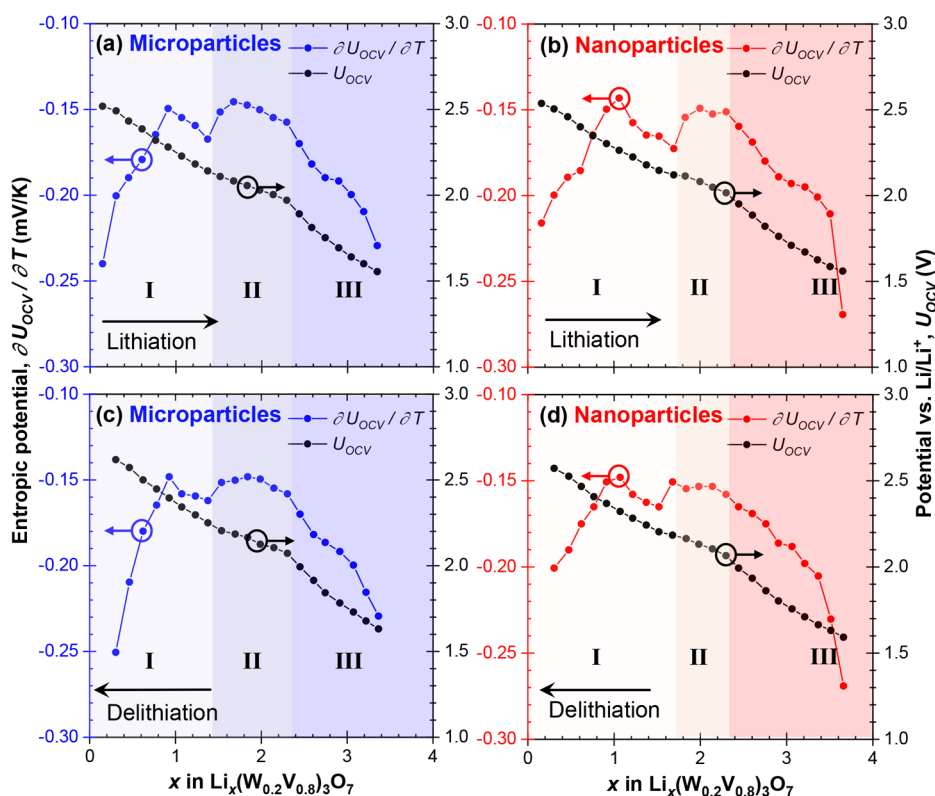


Figure 3. Open-circuit voltage $U_{ocv}(x, T)$ and entropic potential $\partial U_{ocv}(x, T)/\partial T$ of the cell containing electrodes made of $(\text{W}_{0.2}\text{V}_{0.8})_3\text{O}_7$ (a,c) microparticles and (b,d) nanoparticles during (a,b) lithiation and (c,d) delithiation as functions of lithium composition x in $\text{Li}_x(\text{W}_{0.2}\text{V}_{0.8})_3\text{O}_7$ at temperature $T = 20^\circ\text{C}$.

microparticles. Note also that, in both cases, the capacity was larger than the theoretical capacity calculated based on one electron per transition metal. These results demonstrate the ability of $(\text{W}_{0.2}\text{V}_{0.8})_3\text{O}_7$ to engage in multielectron redox reactions, as confirmed previously by X-ray photoelectron spectroscopy (XPS) measurements.¹⁰ Figure 2(d) shows the specific capacity as a function of cycle number for coin cells with electrodes made of $(\text{W}_{0.2}\text{V}_{0.8})_3\text{O}_7$ microparticles and nanoparticles at different C-rates between C/5 and 10C for the same potential window. Here also, the cell made with an electrode consisting of $(\text{W}_{0.2}\text{V}_{0.8})_3\text{O}_7$ nanoparticles featured a larger capacity than that consisting of $(\text{W}_{0.2}\text{V}_{0.8})_3\text{O}_7$ microparticles at any C-rate, as illustrated in Figure S2 of Supporting Information plotting the galvanostatic charge–discharge potential profile at different C-rates ranging between 1C and 10C. Moreover, both electrodes showed impressive fast-charging ability. In fact, at C-rate of 10C, both types of electrodes maintained about 50% of their specific capacity at C/5. In addition, after 20 cycles, they maintained their specific capacity and showed reversibility. Furthermore, for both nanoparticles and microparticles, the charge transfer resistance was not significantly affected by lithium intercalation and remains at a reasonably consistent and low value for all states of charge (see Figure S3 in Supporting Information). The charge transfer resistance in fully lithiated $(\text{W}_{0.2}\text{V}_{0.8})_3\text{O}_7$ microparticles was found to be 103Ω through a Z-fit. This is nearly identical with the charge transfer resistance of fully lithiated $(\text{W}_{0.2}\text{V}_{0.8})_3\text{O}_7$ nanoparticles.¹⁰ The charge transfer resistance is correlated to the resistivity in both materials. Because the crystal and electronic structure of both materials are identical, and independent of particle morphology, we,

therefore, expect the charge transfer resistance to be very similar. Overall, the electrochemical testing was consistent with that reported in our previous study.¹⁰ It is presented here for the sake of completeness and confirms that the samples used in this study show the fast-charging abilities and the superior performance of electrodes made of nanoparticles compared to those made of microparticles.

4.2. $U_{ocv}(x, T)$ and $\partial U_{ocv}(x, T)/\partial T$ Measurements. Figure 3 plots the open-circuit voltage $U_{ocv}(x, T)$ and entropic potential $\partial U_{ocv}(x, T)/\partial T$ measured at 20°C as functions of x composition in $\text{Li}_x(\text{W}_{0.2}\text{V}_{0.8})_3\text{O}_7$ at a C-rate of C/10 during lithiation [Figures 3(a,b)] and delithiation [Figures 3(c,d)] for coin cells with electrodes consisting of $(\text{W}_{0.2}\text{V}_{0.8})_3\text{O}_7$ microparticles [Figures 3(a,c)] and nanoparticles [Figures 3(b,d)]. The trends of both $U_{ocv}(x, T)$ and $\partial U_{ocv}(x, T)/\partial T$ were very similar for both types of electrodes and were almost identical during lithiation and delithiation. These results confirm that the physicochemical phenomena occurring at the $(\text{W}_{0.2}\text{V}_{0.8})_3\text{O}_7$ electrodes were reversible. However, the electrode made of $(\text{W}_{0.2}\text{V}_{0.8})_3\text{O}_7$ nanoparticles was able to accommodate more lithium and featured a larger range of x compositions compared to that with microparticles, as also observed in Figure 2(c).

Three different regions corresponding to different physicochemical phenomena could be identified in Figure 3. In Region I, $U_{ocv}(x, T)$ decreased monotonically indicating lithium insertion in a homogeneous solid solution, as confirmed by *in situ* XRD measurements.¹⁰ This regime was observed for $x < 1.5$ in coin cells with the electrode made of $(\text{W}_{0.2}\text{V}_{0.8})_3\text{O}_7$ microparticles and for $x < 1.7$ in that with the electrode made of nanoparticles. In Region I, $\partial U_{ocv}(x, T)/\partial T$

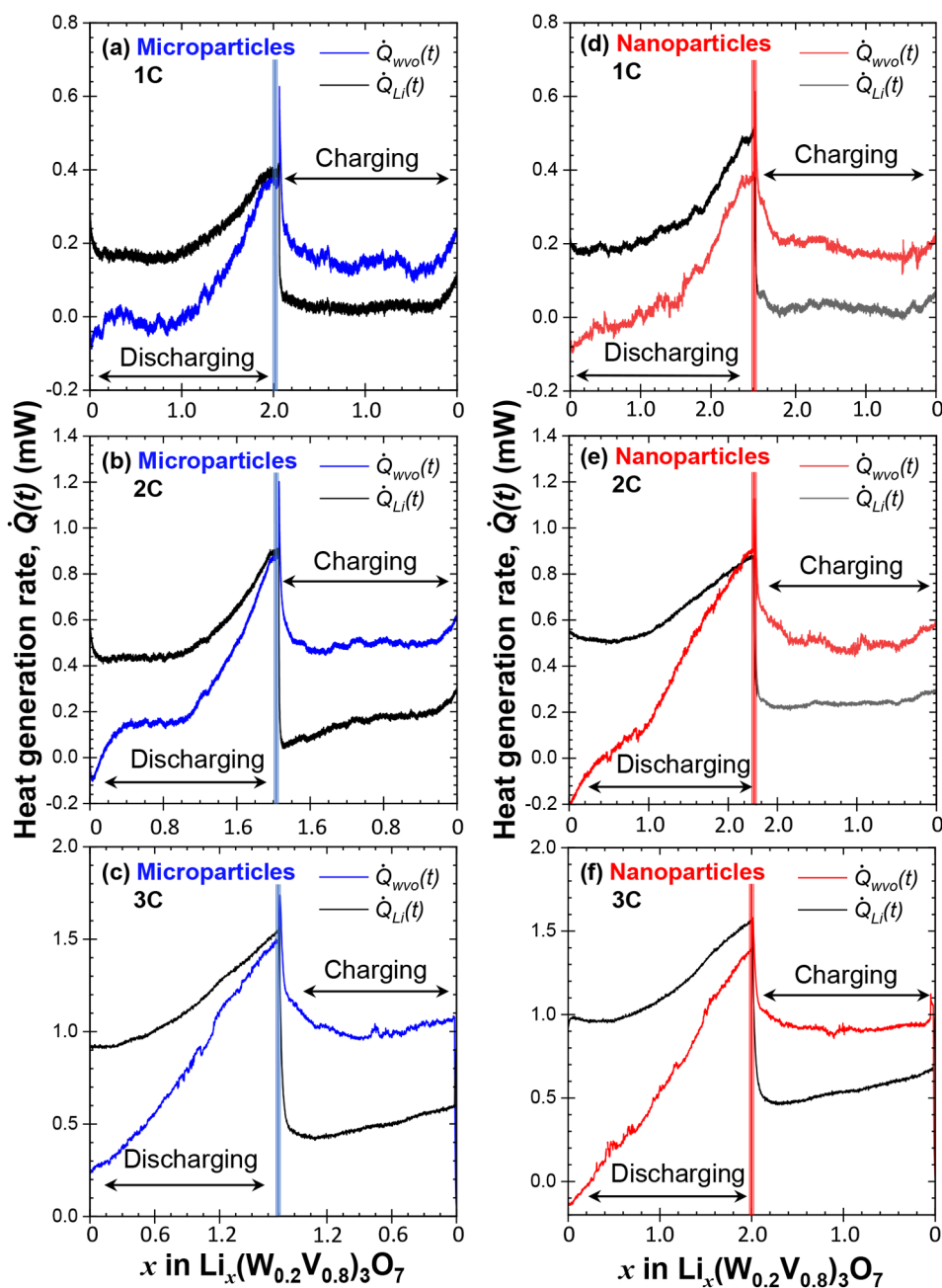


Figure 4. Measured instantaneous heat generation rates $\dot{Q}_{wvo}(t)$ at the $(W_{0.2}V_{0.8})_3O_7$ -based electrodes and $\dot{Q}_{Li}(t)$ at the lithium metal electrode averaged over 5 consecutive cycles as functions of lithium composition x in $Li_x(W_{0.2}V_{0.8})_3O_7$ with potential window ranging from 1.0 to 3.0 V vs Li/Li^+ at C-rates of (a,d) 1C, (b,e) 2C, and (c,f) 3C for $(W_{0.2}V_{0.8})_3O_7$ (a,b,c) microparticles and (d,e,f) nanoparticles.

increased first and then decreased with increasing x , resulting in a local maximum. This behavior could be attributed to the semiconductor to metal transition occurring in $(W_{0.2}V_{0.8})_3O_7$, resulting in a large change in the partial molar electronic entropy. Assuming $(W_{0.2}V_{0.8})_3O_7$ as an ideal intercalation compound, the total entropy $s_{wvo}(x, T)$ of the $(W_{0.2}V_{0.8})_3O_7$ can be expressed as the sum of individual contributions according to¹¹

$$s_{wvo}(x, T) = s_{wvo}^{conf}(x, T) + s_{wvo}^{vib}(x, T) + s^{elec}(x, T) \quad (14)$$

where $s_{wvo}^{conf}(x, T)$, $s_{wvo}^{vib}(x, T)$, and $s_{wvo}^{elec}(x, T)$ are the configurational, vibrational, and electronic entropy of the $(W_{0.2}V_{0.8})_3O_7$

compound, respectively. Therefore, eq 2 can also be expressed as

$$\frac{\partial U_{ocv}(x, T)}{\partial T} = \frac{1}{e} \left[\frac{\partial s_{wvo}^{conf}(x, T)}{\partial x} + \frac{\partial s_{wvo}^{vib}(x, T)}{\partial x} + \frac{\partial s_{wvo}^{elec}(x, T)}{\partial x} - s_{Li}^o(T) \right] \quad (15)$$

A previous study has demonstrated that $\partial s_{wvo}^{conf}(x, T)/\partial x$ decreased monotonically with increasing x .¹¹ In addition, $\partial s_{wvo}^{vib}(x, T)/\partial x$ was independent of x based on the vibrational spectrum of the Li ions approximated by the Einstein model.¹¹

Thus, the trend of $\partial U_{\text{ocv}}(x, T)/\partial T$ leading to a local maximum in Region I was attributed to a change in partial molar electronic entropy $\partial s_{\text{WVO}}^{\text{elec}}(x, T)/\partial x$. For itinerant electrons, the electronic entropy can be expressed as³⁷

$$s^{\text{elec}}(x, T) = -k_{\text{B}} \int [\mathcal{F}(\varepsilon) \ln[\mathcal{F}(\varepsilon)] + [1 - \mathcal{F}(\varepsilon)] \ln[1 - \mathcal{F}(\varepsilon)]] \mathcal{D}^{\text{elec}}(\varepsilon) d\varepsilon \quad (16)$$

where $\mathcal{F}(\varepsilon)$ is the Fermi–Dirac distribution and $\mathcal{D}^{\text{elec}}(\varepsilon)$ is the electronic density of states per unit cell. The electronic entropy depends on the shape of the electronic density of states $\mathcal{D}^{\text{elec}}(\varepsilon)$ and the position of the Fermi level ε_{F} . The majority of Wadley–Roth materials begins as fully oxidized d^0 oxides. Lithiation of these materials effectively serves to dope the material by reducing the transition metals and putting electrons into the d bands, thus lifting the Fermi level. With sufficient lithiation, this is seen to manifest as an insulator to metal transition in $\text{PNb}_3\text{O}_{25}$, supported with both experimental and computational results.^{9,13} Here, $(\text{W}_{0.2}\text{V}_{0.8})_3\text{O}_7$ is unique in that it does not begin fully oxidized and instead contains a small amount of partially reduced V^{4+} . However, the material is not metallic either and can be characterized as a type of semiconductor. The electronic structure of unlithiated $(\text{W}_{0.2}\text{V}_{0.8})_3\text{O}_7$ is analogous to that of low lithiation levels in $\text{PNb}_3\text{O}_{25}$, with the charge density localized on the central corner-connected octahedron.¹⁰ In both cases, more doping, i.e., lithiation, is required to induce a transition to a metallic state, with electron delocalization along the edge-sharing features in both structures. Because of this localization, $s_{\text{WVO}}^{\text{elec}}(x, T)$ was small initially at low x composition when the material was a semiconductor due to the small density of state at the Fermi level.³⁸ However, it increased sharply upon lithiation as the material became a metal and exhibited a large density of state at the Fermi level. Therefore, the local maximum in $\partial U_{\text{ocv}}(x, T)/\partial T$ observed in Region I could be attributed to the change in partial molar electronic entropy $\partial s_{\text{WVO}}^{\text{elec}}(x, T)/\partial x$ due to the semiconductor to metal transition known to occur in this regime (see Supporting Information). In Region II, both $U_{\text{ocv}}(x, T)$ and $\partial U_{\text{ocv}}(x, T)/\partial T$ were approximately constant, confirming a two-phase coexistence region observed previously in *in situ* XRD measurements.¹⁰ The range of x composition in this region was $1.5 \leq x \leq 2.3$ for the electrode composed of microparticles and $1.7 \leq x \leq 2.3$ for that made of nanoparticles. The shorter two-phase coexistence region for the electrode made of nanoparticles can be attributed to the fact that nucleation of a first-order phase transition is often inhibited in smaller particles, and many of these systems are observed to have suppressed phase transition.^{39–41} Moreover, upon two-phase coexistence, lattice mismatch occurs within the particle due to the different lattice parameters associated with two different phases. For a small particle, the lattice mismatch accompanied by two-phase coexistence cannot be compensated internally, thus inhibiting the two-phase coexistence.⁴² For example, LiFePO_4 experiences large volume expansion during two-phase coexistence, leading to notable lattice mismatch within the particle. However, LiFePO_4 particles with mean size less than 140 nm significantly shorten the two-phase coexistence region by avoiding substantial lattice mismatch.⁴³ Finally, in Region III, both $U_{\text{ocv}}(x, T)$ and $\partial U_{\text{ocv}}(x, T)/\partial T$ decreased monotonically, indicating lithium insertion in a homogeneous solid solution. This was consistent with observations from *in situ* XRD

measurements.¹⁰ Region III prevails for $x \geq 2.3$ for both types of electrodes consisting of $(\text{W}_{0.2}\text{V}_{0.8})_3\text{O}_7$ microparticles or nanoparticles.

4.3. Operando Isothermal Calorimetry. **4.3.1. Instantaneous Heat Generation Rates.** Figures 4(a)–4(c) show the instantaneous heat generation rates $\dot{Q}_{\text{WVO}}(t)$ measured at the electrode made of $(\text{W}_{0.2}\text{V}_{0.8})_3\text{O}_7$ microparticles and $\dot{Q}_{\text{Li}}(t)$ measured at the lithium metal counter electrode and averaged over 5 consecutive cycles as functions of lithium composition x in $\text{Li}_x(\text{W}_{0.2}\text{V}_{0.8})_3\text{O}_7$ at 20 °C and at C-rate of (a) 1C, (b) 2C, and (c) 3C, respectively. Similarly, Figures 4(d)–4(f) plot $\dot{Q}_{\text{WVO}}(t)$ measured at the electrode consisting of $(\text{W}_{0.2}\text{V}_{0.8})_3\text{O}_7$ nanoparticles and $\dot{Q}_{\text{Li}}(t)$ at the lithium metal counter electrode averaged over 5 consecutive cycles as functions of x composition at C-rate of (d) 1C, (e) 2C, and (f) 3C, respectively, under the same conditions. The measurements at each electrode were repeatable over many cycles (see Figure S5 in Supporting Information). In addition, the trend and magnitude of $\dot{Q}_{\text{WVO}}(t)$ for both electrodes made of $(\text{W}_{0.2}\text{V}_{0.8})_3\text{O}_7$ microparticles and nanoparticles were very similar. In both cases, $\dot{Q}_{\text{WVO}}(t)$ was small at the beginning of discharging at low x composition when $(\text{W}_{0.2}\text{V}_{0.8})_3\text{O}_7$ particles were electrically conductive.¹⁰ However, $\dot{Q}_{\text{WVO}}(t)$ increased rapidly due to the increase in charge transfer resistance with increasing x composition in $\text{Li}_x(\text{W}_{0.2}\text{V}_{0.8})_3\text{O}_7$ upon discharging (lithiation).¹⁰ In addition, $\dot{Q}_{\text{WVO}}(t)$ for electrodes composed of $(\text{W}_{0.2}\text{V}_{0.8})_3\text{O}_7$ nanoparticles and microparticles featured a small plateau-like region upon discharging at C-rates of 1C and 2C. Interestingly, the x composition of the plateau region in the $\dot{Q}_{\text{WVO}}(t)$ ranged between 0.5 and 1.2, corresponding to the end of Region I where $\partial U_{\text{ocv}}(x, T)/\partial T$ decreased with increasing x identified in Figure 3. As previously discussed, $\partial U_{\text{ocv}}(x, T)/\partial T$ is directly related to the reversible heat generation rate [eq 5]. In fact, decreasing $\partial U_{\text{ocv}}(x, T)/\partial T$ observed in this x composition could diminish the reversible heat generation rate, thus resulting in a plateau in $\dot{Q}_{\text{WVO}}(t)$. However, at C-rates of 3C, this feature was not apparent, possibly due to the fact that the irreversible heat generation was much larger than the reversible heat generation and dominated the total heat generation rate.

4.3.2. Time-Averaged Heat Generation Rates. Figure 5 shows the time-averaged irreversible heat generation rates and $\bar{Q}_{\text{irr, Li}}$ (eq 13) averaged over 5 consecutive cycles. The error bars represent two standard deviations or a 95% confidence interval. Fitting of $\bar{Q}_{\text{irr, Li}}$ with respect to current I at the metallic Li electrode yields $\bar{Q}_{\text{irr, Li}} \propto I^2$. In other words, the irreversible heat generation was dominated by Joule heating since the resistance of the metallic Li electrode was constant. Importantly, $\bar{Q}_{\text{irr, WVO}}$ in the electrode made of $(\text{W}_{0.2}\text{V}_{0.8})_3\text{O}_7$ microparticles became slightly but systematically larger than that in the electrode made of nanoparticles at C-rates of 2C and 3C, despite the fact that the applied current was larger for the nanoparticle-based electrode. This behavior could be attributed to the fact that an electrode with larger particles generally features larger electrical resistivity, thus increasing Joule heating.⁴⁴ The enthalpy of mixing also contributed to the irreversible heat generation and increased with increasing particle size due to diffusion limitation, particularly at high C-

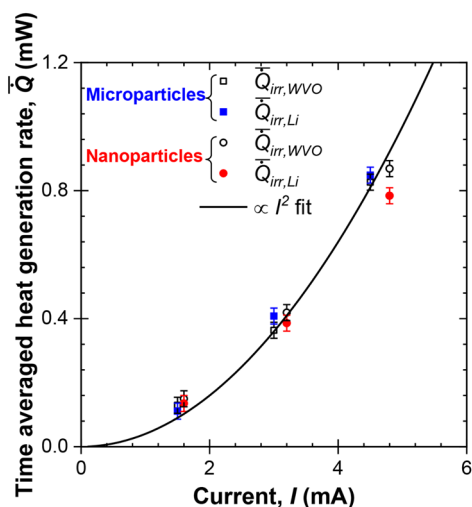


Figure 5. Time-averaged irreversible heat generation rates $\bar{Q}_{\text{irr,WVO}}$ and $\bar{Q}_{\text{irr,Li}}$, as functions of applied current I based on the isothermal *operando* calorimetry measurements at temperature $T = 20$ °C.

rates.^{13,28} Decreasing the particle size reduced the lithium concentration gradient formed within the particles and thus

reduced the irreversible heat of mixing (eq 6).^{29,31} Here, $\bar{Q}_{\text{irr,WVO}}$ at the $(\text{W}_{0.2}\text{V}_{0.8})_3\text{O}_7$ -based electrodes made of microparticles and nanoparticles were similar at C-rate of 1C. This observation could possibly be attributed to the fact that the contribution of enthalpy of mixing to the irreversible heat generation rate is small at relatively low C-rates. Furthermore, the mass loading of $(\text{W}_{0.2}\text{V}_{0.8})_3\text{O}_7$ nanoparticles was larger than that of microparticles. Thus, the applied current was also larger for the electrode consisting of nanoparticles.

4.3.3. Heat Generation Rate of a Full Cell. Figure 6 plots the total instantaneous heat generation rate given by $\dot{Q}_T(x) = \dot{Q}_{\text{Li}}(x) + \dot{Q}_{\text{WVO}}(x)$ measured in the entire cell with electrodes made of $(\text{W}_{0.2}\text{V}_{0.8})_3\text{O}_7$ in the form of (a,b) microparticles and (c,d) nanoparticles as functions of lithium composition x at C-rate of 1C during (a,c) lithiation and (b,d) delithiation, respectively. It also shows the contributions from Joule heating $\dot{Q}_J(x)$ and the reversible entropic heat generation $\dot{Q}_{\text{rev}}(x)$ predicted by eqs 4 and 5, respectively.^{5,20,27,28} Here, $\dot{Q}_{\text{rev}}(x)$ was exothermic during lithiation and endothermic during delithiation, as expected from the sign of $\partial U_{\text{ocv}}(x, T)/\partial T$ shown in Figure 3. The predictions of $\dot{Q}_J(x) + \dot{Q}_{\text{rev}}(x)$ from the measured current and voltage agreed well with the

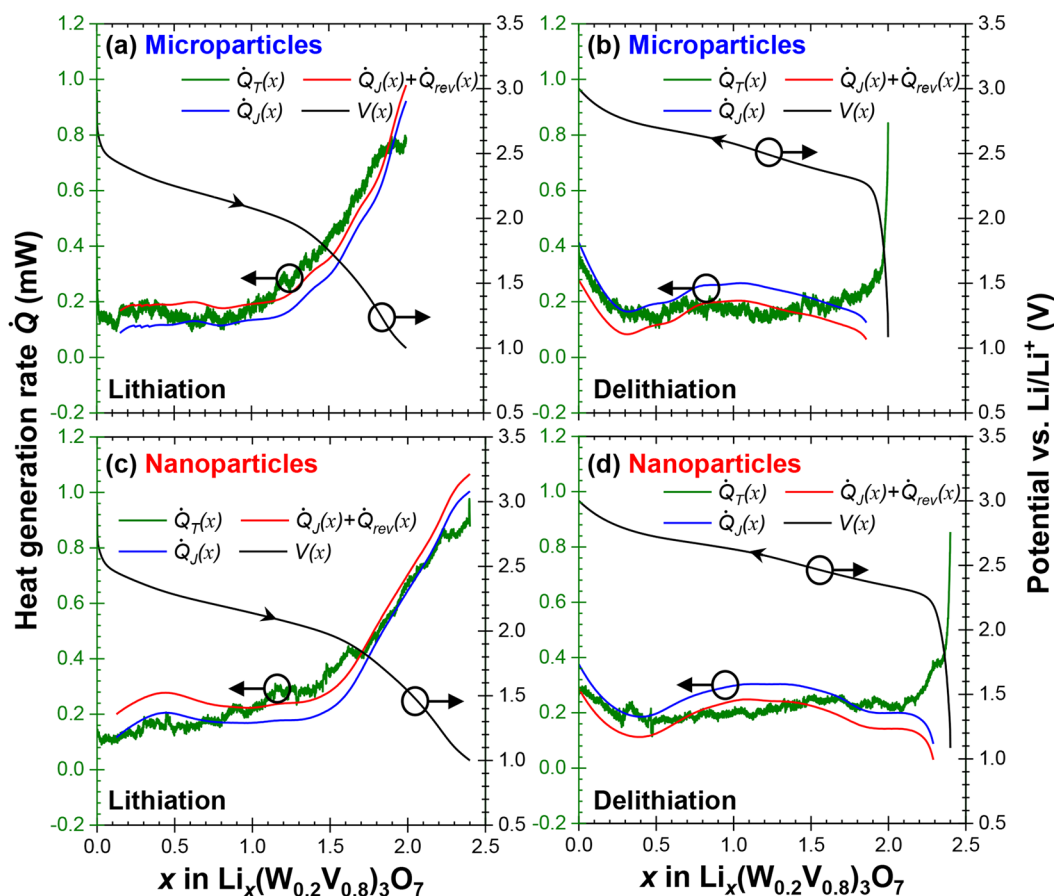


Figure 6. Measured total heat generation rate $\dot{Q}_T(x) = \dot{Q}_{\text{Li}}(x) + \dot{Q}_{\text{WVO}}(x)$ and predictions of the heat generation rates $\dot{Q}_J(x)$ and $\dot{Q}_J(x) + \dot{Q}_{\text{rev}}(x)$ calculated based on eqs 4 and 5 along with the measured voltage $V(x)$ upon (a,c) lithiation and (b,d) delithiation at C-rate of 1C for a cell containing electrodes consisting of (a,b) $(\text{W}_{0.2}\text{V}_{0.8})_3\text{O}_7$ microparticles synthesized by the solid-state method and (c,d) $(\text{W}_{0.2}\text{V}_{0.8})_3\text{O}_7$ nanoparticles synthesized by sol-gel with a freeze-drying method at temperature $T = 20$ °C.

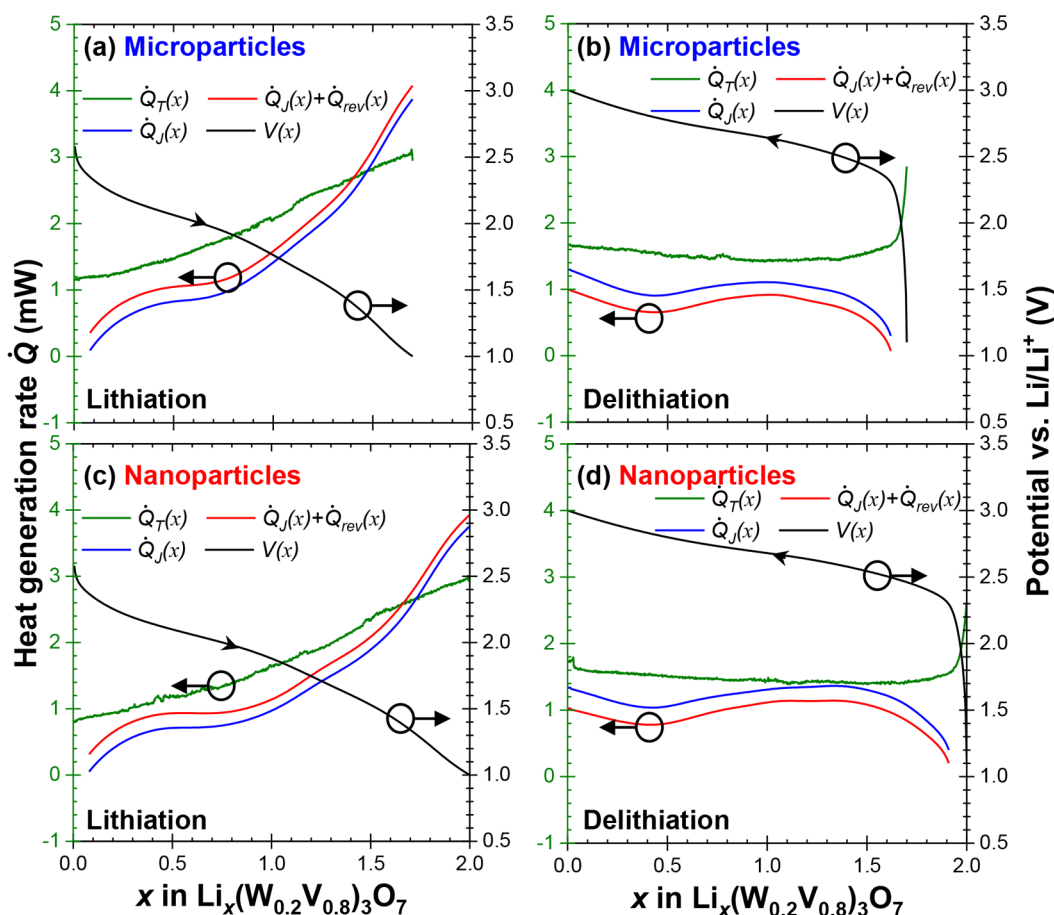


Figure 7. Measured total heat generation rate $\dot{Q}_T(x) = \dot{Q}_{\text{Li}}(x) + \dot{Q}_{\text{WVO}}(x)$ and predictions of the heat generation rates $\dot{Q}_J(x)$ and $\dot{Q}_J(x) + \dot{Q}_{\text{rev}}(x)$ calculated based on eqs 4 and 5 along with the measured voltage $V(x)$ upon (a,c) lithiation and (b,d) delithiation at C-rate of 3C for a cell containing electrodes consisting of (a,b) $(\text{W}_{0.2}\text{V}_{0.8})_3\text{O}_7$ microparticles synthesized by the solid-state method and (c,d) $(\text{W}_{0.2}\text{V}_{0.8})_3\text{O}_7$ nanoparticles synthesized by sol-gel with a freeze-drying method at temperature $T = 20^\circ\text{C}$.

measured total heat generation rate $\dot{Q}_T(x)$ for lithiation. The differences between the predictions of $\dot{Q}_J(x) + \dot{Q}_{\text{rev}}(x)$ and the measured $\dot{Q}_T(x)$ were larger during delithiation than lithiation possibly due to relatively slow kinetics of delithiation compared to that of lithiation, as observed in the apparent diffusion coefficient of Li^+ ions in the $(\text{W}_{0.2}\text{V}_{0.8})_3\text{O}_7$ electrode (see Supporting Information).

To understand what happens when the cell is cycled faster, Figure 7 plots the total instantaneous heat generation $\dot{Q}_T(x)$ measured in the entire cell with electrodes consisting of $(\text{W}_{0.2}\text{V}_{0.8})_3\text{O}_7$ in the form of (a,b) microparticles and (c,d) nanoparticles as functions of lithium composition x at a C-rate of 3C during (a,c) lithiation and (b,d) delithiation, respectively. Again, at 3C the difference between the predictions of $\dot{Q}_J(x) + \dot{Q}_{\text{rev}}(x)$ and the measured $\dot{Q}_T(x)$ was larger during delithiation than lithiation. Moreover, the differences between the predictions of $\dot{Q}_J(x) + \dot{Q}_{\text{rev}}(x)$ and the measurements of $\dot{Q}_T(x)$ were larger at a C-rate of 3C than at 1C (Figure 6). This can be attributed to the enthalpy of mixing \dot{Q}_{mix} , according to eq 3. The heat generation rate $\dot{Q}_{\text{mix}}(x)$ should increase with increasing C-rates due to an

increase in the lithium concentration gradients developed within the electrode due to diffusion limitation.^{29,31}

4.3.4. Energy Balance. Figure 8 presents the electrical energy losses $\Delta E_e/C_m$ (eq 9) at C-rates of 1C, 2C, and 3C along with the predicted Joule heating Q_J/C_m (eq 8) and the total thermal energy Q_T/C_m per specific capacity C_m dissipated in the entire cell measured experimentally for electrodes made of $(\text{W}_{0.2}\text{V}_{0.8})_3\text{O}_7$ (a) microparticles and (b) nanoparticles, respectively. It is worth noting that the cell-specific capacity was larger for the electrodes made of $(\text{W}_{0.2}\text{V}_{0.8})_3\text{O}_7$ nanoparticles than that made of microparticles. Indeed, specific capacity C_m was measured to be 155 mAh/g at C-rate of 1C, 140 mAh/g at 2C, and 130 mAh/g at 3C for the electrodes made of microparticles and 200 mAh/g at C-rate of 1C, 175 mAh/g at 2C, and 160 mAh/g at 3C for the electrodes made of nanoparticles. In both cells, $\Delta E_e/C_m$ increased with increasing C-rate due to the associated increase in the overpotential $[V(x, T) - U^{\text{avg}}(x, T)]$.^{45,46} Moreover, the specific electrical energy losses $\Delta E_e/C_m$ due to the hysteretic voltage profile were within 5% of the independently measured total specific thermal energy, Q_T/C_m , dissipated over a cycle. In other words, the electrical energy losses were dissipated entirely in the form of heat so that $\Delta E_e/C_m = Q_T/C_m$. Furthermore, the dissipated energy $\Delta E_e/C_m$ per unit of specific capacity was smaller for a cell with the electrode consisting of

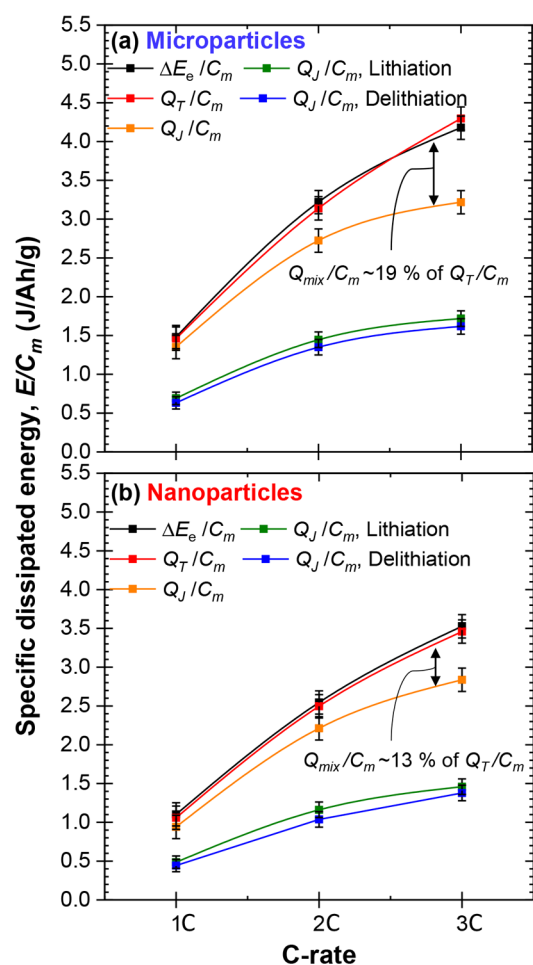


Figure 8. Measured specific net electrical energy losses $\Delta E_e/C_m$ and total specific thermal energy dissipated Q_T/C_m averaged over the first five charging–discharging cycles as well as predicted contributions from Joule heating Q_J/C_m during lithiation and delithiation for a cell made of an electrode consisting of $(W_{0.2}V_{0.8})_3O_7$ (a) microparticles synthesized by the solid-state method and (b) nanoparticles synthesized by sol–gel with a freeze-drying method. The enthalpy of mixing corresponds to $Q_{mix}/C_m = Q_T/C_m - Q_J/C_m = \Delta E_e/C_m - Q_J/C_m$.

$(W_{0.2}V_{0.8})_3O_7$ nanoparticles than that of microparticles. Thus, the electrode made of nanoparticles was energetically more efficient and dissipated less electrical energy than that made of microparticles. Averaging Q_{rev}/C_m over a cycle yields $Q_{rev}/C_m \approx 0$. Thus, the difference between Q_T/C_m and Q_J/C_m corresponded to the heat dissipated in the form of enthalpy of mixing, i.e., $Q_{mix}/C_m = Q_T/C_m - Q_J/C_m$. In both cells, the contribution of the enthalpy of mixing to the total energy dissipated increased with increasing C-rate. For a cell with electrodes consisting of $(W_{0.2}V_{0.8})_3O_7$ microparticles, Q_{mix}/C_m reached 19% at C-rate of 3C compared with 13% for an electrode made of $(W_{0.2}V_{0.8})_3O_7$ nanoparticles. These calorimetry measurements thus demonstrated that using nanoparticles instead of microparticles made it kinetically more favorable for lithium ions to intercalate in $(W_{0.2}V_{0.8})_3O_7$ and resulted in smaller enthalpy of mixing and overall energy dissipation. These two systems show nearly identical behavior in almost all other respects, making this an ideal system for isolating the effects of particle size on enthalpy of mixing and heat dissipation.

5. CONCLUSION

This study investigated the effect of particle size of the Wadsley–Roth compound $(W_{0.2}V_{0.8})_3O_7$ on the thermodynamic properties and heat generation of battery cells. Galvanostatic cycling confirmed that the electrode made of $(W_{0.2}V_{0.8})_3O_7$ nanoparticles synthesized by the sol–gel method combined with freeze-drying featured larger capacity and better capacity retention at high C-rates than that made of $(W_{0.2}V_{0.8})_3O_7$ microparticles synthesized by the solid-state method. Entropic potential measurements confirmed the phase transition identified previously from *in situ* XRD measurements. They also identified the semiconductor to metal transition occurring at low lithium composition.¹⁰ Furthermore, entropic potential measurements showed that the $(W_{0.2}V_{0.8})_3O_7$ nanoparticles underwent a two-phase coexistence region over a narrower range of x compositions possibly due to inhibition of the phase transition caused by their nanoscale size. Isothermal *operando* calorimetry measurements demonstrated that the heat generation rate increased at the $(W_{0.2}V_{0.8})_3O_7$ -based electrode upon lithiation due to an increase in charge transfer resistance. Moreover, the time-averaged irreversible heat generation rate and the enthalpy of mixing were smaller at the electrode made of nanoparticles than at that made of the microparticles particularly at high C-rates. Similarly, the dissipated electrical energy per unit of specific capacity was smaller for a cell with electrodes made of $(W_{0.2}V_{0.8})_3O_7$ nanoparticles than those made of microparticles due to reduced concentration gradients and thus reduced enthalpy of mixing. These results demonstrate that using electrodes consisting of nanoparticles is energetically more efficient thanks to more kinetically favorable lithium-ion intercalation.

■ ASSOCIATED CONTENT

Supporting Information

The Supporting Information is available free of charge at <https://pubs.acs.org/doi/10.1021/acsaem.2c03150>.

X-ray fluorescence spectrometry data; b -value analysis; electrochemical impedance spectroscopy measurements; schematics elucidating insulator to metal transition; apparent lithium diffusion coefficient (PDF)

■ AUTHOR INFORMATION

Corresponding Author

Laurent Pilon – Mechanical and Aerospace Engineering Department, Henry Samueli School of Engineering and Applied Science, University of California, Los Angeles, California 90095, United States; California NanoSystems Institute and Institute of the Environment and Sustainability, University of California, Los Angeles, Los Angeles, California 90095, United States; orcid.org/0000-0001-9459-8207; Phone: +1 (310)-206-5598; Email: pilon@seas.ucla.edu; Fax: +1 (310)-206-2302

Authors

Sun Woong Baek – Mechanical and Aerospace Engineering Department, Henry Samueli School of Engineering and Applied Science, University of California, Los Angeles, California 90095, United States
Kira E. Wyckoff – Materials Department, and Materials Research Laboratory, University of California, Santa Barbara, California 93106, United States

Daniel D. Robertson – Department of Chemistry and Biochemistry, University of California, Los Angeles, California 93106, United States

Matevž Frajnkovič – Mechanical and Aerospace Engineering Department, Henry Samueli School of Engineering and Applied Science, University of California, Los Angeles, California 90095, United States

Yucheng Zhou – Mechanical and Aerospace Engineering Department, Henry Samueli School of Engineering and Applied Science, University of California, Los Angeles, California 90095, United States

Sarah H. Tolbert – Department of Chemistry and Biochemistry, University of California, Los Angeles, California 93106, United States; California NanoSystems Institute, University of California, Los Angeles, Los Angeles, California 90095, United States; Present Address: Material Science and Engineering Department, University of California, Los Angeles, Los Angeles, California 90095, United States; orcid.org/0000-0001-9969-1582

Ram Seshadri – Materials Department, and Materials Research Laboratory, University of California, Santa Barbara, California 93106, United States; Department of Chemistry and Biochemistry, University of California, Santa Barbara, California 93106, United States; orcid.org/0000-0001-5858-4027

Complete contact information is available at:
<https://pubs.acs.org/10.1021/acsaem.2c03150>

Notes

The authors declare no competing financial interest.

ACKNOWLEDGMENTS

This work was supported as part of the Center for Synthetic Control Across Length-scales for Advancing Rechargeables (SCALAR), an Energy Frontier Research Center funded by the U.S. Department of Energy, Office of Science, Basic Energy Sciences under Award # DE-SC0019381. This work made use of MRL Shared Experimental Facilities that are supported by the MRSEC Program of the NSF under Award No. DMR 1720256, a member of the NSF-funded Materials Research Facilities Network (www.mrfn.org).

REFERENCES

- (1) Mizushima, K.; Jones, P. C.; Wiseman, P. J.; Goodenough, J. B. Li_xCoO_2 ($0 < x < -1$): A new cathode material for batteries of high energy density. *Mater. Res. Bull.* **1980**, *15*, 783–789.
- (2) Yuan, L.-X.; Wang, Z.-H.; Zhang, W.-X.; Hu, X.-L.; Chen, J.-T.; Huang, Y.-H.; Goodenough, J. B. Development and challenges of LiFePO_4 cathode material for lithium-ion batteries. *Energy Environ. Sci.* **2011**, *4*, 269–284.
- (3) Lee, S.; Oshima, Y.; Hosono, E.; Zhou, H.; Kim, K.; Chang, H. M.; Kanno, R.; Takayanagi, K. Phase transitions in a LiMn_2O_4 nanowire battery observed by *operando* electron microscopy. *ACS Nano* **2015**, *9*, 626–632.
- (4) Liu, Y.; Zhu, Y.; Cui, Y. Challenges and opportunities towards fast-charging battery materials. *Nature Energy* **2019**, *4*, 540–550.
- (5) Baek, S. W.; Wyckoff, K. E.; Butts, D. M.; Bienz, J.; Likitchchawankun, A.; Preefer, M. B.; Frajnkovič, M.; Dunn, B. S.; Seshadri, R.; Pilon, L. *Operando* Calorimetry Informs the Origin of Rapid Rate Performance in Microwave-prepared TiNb_2O_7 Electrodes. *J. Power Sources* **2021**, *490*, 229537.
- (6) Roth, R. S.; Wadsley, A. D.; Andersson, S. The crystal structure of $\text{PNb}_3\text{O}_{25}$. *Acta Crystallogr.* **1965**, *18*, 643–647.

- (7) Zhu, X.; Xu, J.; Luo, Y.; Fu, Q.; Liang, G.; Luo, L.; Chen, Y.; Lin, C.; Zhao, X. S. $\text{MoNb}_{12}\text{O}_{33}$ as a new anode material for high-capacity, safe, rapid and durable Li^+ storage: structural characteristics, electrochemical properties and working mechanisms. *Journal of Material Chemistry A* **2019**, *7*, 6522–6532.

- (8) Griffith, K. J.; Seymour, I. D.; Hope, M. A.; Butala, M. M.; Lamontagne, L. K.; Preefer, M. B.; Kocer, C. P.; Henkelman, G.; Morris, A. J.; Cliffe, M. J.; et al. Ionic and electronic conduction in TiNb_2O_7 . *J. Am. Chem. Soc.* **2019**, *141*, 16706–16725.

- (9) Preefer, M. B.; Saber, M.; Wei, Q.; Bashian, N. H.; Bocarsly, J. D.; Zhang, W.; Lee, G.; Milam-Guerrero, J.; Howard, E. S.; Vincent, R. C.; Melot, B. C.; Van der Ven, A.; Seshadri, R.; Dunn, B. S. Multielectron Redox and Insulator-to-Metal Transition upon Lithium Insertion in the Fast-Charging, Wadsley-Roth Phase $\text{PNb}_3\text{O}_{25}$. *Chem. Mater.* **2020**, *32*, 4553–4563.

- (10) Wyckoff, K. E.; Robertson, D. D.; Preefer, M. B.; Teicher, S. M.; Bienz, J.; Kautzsch, L.; Mates, T. E.; Cooley, J. A.; Tolbert, S. H.; Seshadri, R. High-Capacity Li^+ Storage through Multielectron Redox in the Fast-Charging Wadsley–Roth Phase ($\text{W}_{0.2}\text{V}_{0.8}$) $_3\text{O}_7$. *Chem. Mater.* **2020**, *32*, 9415–9424.

- (11) Baek, S. W.; Saber, M.; Van der Ven, A.; Pilon, L. Thermodynamic Analysis and Interpretative Guide to Entropic Potential Measurements of Lithium-Ion Battery Electrodes. *J. Phys. Chem. C* **2022**, *126*, 6096–6110.

- (12) Munteshari, O.; Lau, J.; Krishnan, A.; Dunn, B. S.; Pilon, L. Isothermal calorimeter for measurements of time-dependent heat generation rate in individual supercapacitor electrodes. *J. Power Sources* **2018**, *374*, 257–268.

- (13) Baek, S. W.; Preefer, M. B.; Saber, M.; Zhai, K.; Frajnkovič, M.; Zhou, Y.; Dunn, B. S.; Van der Ven, A.; Seshadri, R.; Pilon, L. Potentiometric entropy and *operando* calorimetric measurements reveal fast charging mechanisms in $\text{PNb}_3\text{O}_{25}$. *J. Power Sources* **2022**, *520*, 230776.

- (14) Van der Ven, A.; Bhattacharya, J.; Belak, A. A. Understanding Li diffusion in Li-intercalation compounds. *Acc. Chem. Res.* **2013**, *46*, 1216–1225.

- (15) Chase, M. *NIST-JANAF Thermochemical Tables*, 4th ed.; American Institute of Physics: New York, NY, USA, 1998.

- (16) Giel, H.; Henriques, D.; Bourne, G.; Markus, T. Investigation of the heat generation of a commercial 2032 (LiCoO_2) coin cell with a novel differential scanning battery calorimeter. *J. Power Sources* **2018**, *390*, 116–126.

- (17) Du Pasquier, A.; Disma, F.; Bowmer, T.; Gozdz, A.; Amatucci, G.; Tarascon, J.-M. Differential scanning calorimetry study of the reactivity of carbon anodes in plastic Li-ion batteries. *J. Electrochem. Soc.* **1998**, *145*, 472–477.

- (18) Wang, Y.; Zaghbi, K.; Guerfi, A.; Bazito, F.; Torresi, R.; Dahn, J. Accelerating rate calorimetry studies of the reactions between ionic liquids and charged lithium ion battery electrode materials. *Electrochim. Acta* **2007**, *52*, 6346–6352.

- (19) Feng, X.; Fang, M.; He, X.; Ouyang, M.; Lu, L.; Wang, H.; Zhang, M. Thermal runaway features of large format prismatic lithium ion battery using extended volume accelerating rate calorimetry. *J. Power Sources* **2014**, *255*, 294–301.

- (20) Assat, G.; Glazier, S. L.; Delacourt, C.; Tarascon, J.-M. Probing the thermal effects of voltage hysteresis in anionic redox-based lithium-rich cathodes using isothermal calorimetry. *Nature Energy* **2019**, *4*, 647–656.

- (21) Likitchchawankun, A.; Whang, G.; Lau, J.; Munteshari, O.; Dunn, B. S.; Pilon, L. Effect of temperature on irreversible and reversible heat generation rates in ionic liquid-based electric double layer capacitors. *Electrochim. Acta* **2020**, *338*, 135802.

- (22) Munteshari, O.; Borenstein, A.; DeBlock, R. H.; Lau, J.; Whang, G.; Zhou, Y.; Likitchchawankun, A.; Kaner, R. B.; Dunn, B.; Pilon, L. *Inoperando* calorimetric measurements for activated carbon electrodes in ionic liquid electrolytes under large potential windows. *ChemSusChem* **2020**, *13*, 1013–1026.

- (23) Likitchchawankun, A.; Kundu, A.; Munteshari, O.; Fisher, T. S.; Pilon, L. Heat generation in all-solid-state supercapacitors with

graphene electrodes and gel electrolytes. *Electrochim. Acta* **2019**, *303*, 341–353.

(24) Munteshari, O.; Lau, J.; Likitchawankun, A.; Mei, B.-A.; Choi, C. S.; Butts, D.; Dunn, B. S.; Pilon, L. Thermal signature of ion intercalation and surface redox reactions mechanisms in model pseudocapacitive electrodes. *Electrochim. Acta* **2019**, *307*, 512–524.

(25) Likitchawankun, A.; DeBlock, R. H.; Whang, G.; Munteshari, O.; Frajnkovič, M.; Dunn, B. S.; Pilon, L. Heat generation in electric double layer capacitors with neat and diluted ionic liquid electrolytes under large potential window between 5 and 80 °C. *J. Power Sources* **2021**, *488*, 229368.

(26) Munteshari, O.; Lau, J.; Ashby, D. S.; Dunn, B. S.; Pilon, L. Effects of constituent materials on heat generation in individual EDLC electrodes. *J. Electrochem. Soc.* **2018**, *165*, A1547–A1557.

(27) Liu, G.; Ouyang, M.; Lu, L.; Li, J.; Han, X. Analysis of the heat generation of lithium-ion battery during charging and discharging considering different influencing factors. *J. Therm. Anal. Calorim.* **2014**, *116*, 1001–1010.

(28) Newman, J.; Thomas, K. E.; Hafezi, H.; Wheeler, D. R. Modeling of lithium-ion batteries. *J. Power Sources* **2003**, *119*, 838–843.

(29) Thomas, K. E.; Newman, J. Thermal Modeling of Porous Insertion Electrodes. *J. Electrochem. Soc.* **2003**, *150*, A176–A192.

(30) Lu, W.; Prakash, J. *In situ* measurements of heat generation in a Li/mesocarbon microbead half-cell. *J. Electrochem. Soc.* **2003**, *150*, A262–A266.

(31) Thomas, K.; Newman, J. Heats of mixing and of entropy in porous insertion electrodes. *J. Power Sources* **2003**, *119*, 844–849.

(32) Smith, K.; Wang, C.-Y. Power and thermal characterization of a lithium-ion battery pack for hybrid-electric vehicles. *J. Power Sources* **2006**, *160*, 662–673.

(33) Zhou, Y.; Le Calvez, E.; Baek, S. W.; Frajnkovič, M.; Douard, C.; Gautron, E.; Crosnier, O.; Brousse, T.; Pilon, L. Effect of particle size on thermodynamics and lithium ion transport in electrodes made of Ti₂Nb₂O₉ microparticles or nanoparticles. *Energy Storage Materials* **2022**, *52*, 371–385.

(34) Heurung, G.; Gruehn, R. High-resolution transmission electron microscopy—Investigation of vanadium-tungsten oxides prepared by chemical transport reactions. *J. Solid State Chem.* **1984**, *55*, 337–343.

(35) Ko, J. S.; Lai, C.-H.; Long, J. W.; Rolison, D. R.; Dunn, B.; Nelson Weker, J. Differentiating double-layer, pseudocapacitance, and battery-like mechanisms by analyzing impedance measurements in three dimensions. *ACS Appl. Mater. Interfaces* **2020**, *12*, 14071–14078.

(36) Kim, T.; Choi, W.; Shin, H.-C.; Choi, J.-Y.; Kim, J.; Park, M.-S.; Yoon, W.-S. Applications of voltammetry in lithium ion battery research. *Journal of Electrochemical Science and Technology* **2020**, *11*, 14–25.

(37) Wallace, D. *Thermodynamics of Crystals*; Dover: Mineola, NY, USA, 1998.

(38) Zhou, F.; Maxisch, T.; Ceder, G. Configurational electronic entropy and the phase diagram of mixed-valence oxides: the case of Li_xFePO₄. *Phys. Rev. Lett.* **2006**, *97*, 155704.

(39) Kim, D.-H.; Kim, J. Synthesis of LiFePO₄ nanoparticles in polyol medium and their electrochemical properties. *Electrochem. Solid-State Lett.* **2006**, *9*, A439–A442.

(40) Yang, Z.; Choi, D.; Kerisit, S.; Rosso, K. M.; Wang, D.; Zhang, J.; Graff, G.; Liu, J. Nanostructures and lithium electrochemical reactivity of lithium titanates and titanium oxides: A review. *J. Power Sources* **2009**, *192*, 588–598.

(41) Cook, J. B.; Lin, T. C.; Kim, H.-S.; Siordia, A.; Dunn, B. S.; Tolbert, S. H. Suppression of electrochemically driven phase transitions in nanostructured MoS₂ pseudocapacitors probed using *operando* X-ray diffraction. *ACS Nano* **2019**, *13*, 1223–1231.

(42) Zhao, Y.; De Jesus, L. R.; Stein, P.; Horrocks, G. A.; Banerjee, S.; Xu, B.-X. Modeling of phase separation across interconnected electrode particles in lithium-ion batteries. *RSC Adv.* **2017**, *7*, 41254–41264.

(43) Li, D.; Zhou, H. Two-phase transition of Li-intercalation compounds in Li-ion batteries. *Mater. Today* **2014**, *17*, 451–463.

(44) Nagata, K.; Iwabuki, H.; Nigo, H. Effect of particle size of graphites on electrical conductivity of graphite/polymer composite. *Compos. Interfaces* **1998**, *6*, 483–495.

(45) Ecker, M.; Gerschler, J. B.; Vogel, J.; Käbitz, S.; Hust, F.; Dechent, P.; Sauer, D. U. Development of a lifetime prediction model for lithium-ion batteries based on extended accelerated aging test data. *J. Power Sources* **2012**, *215*, 248–257.

(46) Andre, D.; Meiler, M.; Steiner, K.; Wimmer, C.; Soczka-Guth, T.; Sauer, D. U. Characterization of high-power lithium-ion batteries by electrochemical impedance spectroscopy. I. Experimental investigation. *J. Power Sources* **2011**, *196*, 5334–5341.

Recommended by ACS

Hybrid All-Solid-State Thin-Film Micro-supercapacitor Based on a Pseudocapacitive Amorphous TiO₂ Electrode

Valentin Sallaz, Sami Oukassi, *et al.*

DECEMBER 21, 2022
ACS APPLIED ENERGY MATERIALS

READ 

Effect of Nanoparticles in LiFePO₄ Cathode Material Using Organic/Inorganic Composite Solid Electrolyte for All-Solid-State Batteries

Young-Woong Song, Jinsub Lim, *et al.*

DECEMBER 19, 2022
LANGMUIR

READ 

Overcoming the Interfacial Challenges of LiFePO₄ in Inorganic All-Solid-State Batteries

Ashley Cronk, Ying Shirley Meng, *et al.*

JANUARY 03, 2023
ACS ENERGY LETTERS

READ 

Reversible Electrochemical Lithium Cycling in a Vanadium(IV)- and Niobium(V)-Based Wadsley–Roth Phase

Erick A. Lawrence, Huiwen Ji, *et al.*

APRIL 18, 2023
CHEMISTRY OF MATERIALS

READ 

Get More Suggestions >